University of Dundee

Intrinsic enzyme-like activity of magnetite particles is enhanced by cultivation with Trichoderma guizhouense

Chi, Zhi-Lai; Zhao, Xiang-Yang; Chen, Ya-Ling; Hao, Jia-Long; Yu, Guang-Hui; Goodman, Bernard A

Document Version
Peer reviewed version

[Link to publication in Discovery Research Portal](#)

Intrinsic enzyme-like activity of magnetite particles is enhanced by cultivation with *Trichoderma guizhouense*

Zhi-Lai Chi,[1,‡] Xiang-Yang Zhao,[1,‡] Ya-Ling Chen,[1,2] Jia-Long Hao,[3] Guang-Hui Yu,[1,2,*] Bernard A. Goodman,[4] Geoffrey Michael Gadd,[5,6]

[1] *Jiangsu Provincial Key Lab for Organic Solid Waste Utilization, College of Resource & Environmental Sciences, Nanjing Agricultural University, Nanjing 210095, China*

[2] *Institute of Surface-Earth System Science, School of Earth System Science, Tianjin University, Tianjin 300072, China*

[3] *Key Laboratory of Earth and Planetary Physics, Institute of Geology and Geophysics, Chinese Academy of Sciences, Beijing 100029, China*

[4] *College of Physical Science and Technology, Guangxi University, Nanning 530004, China*

[5] *Geomicrobiology Group, School of Life Sciences, University of Dundee, Dundee DD1 5EH, Scotland, UK*

[6] *State Key Laboratory of Heavy Oil Processing, Beijing Key Laboratory of Oil and Gas Pollution Control, College of Chemical Engineering and Environment, China University of Petroleum, Beijing 102249, China*

Running title: Peroxidase activity of fungal-derived minerals

*For correspondence. Email: yuguanghui@njau.edu.cn or yuguanghui@tju.edu.cn.

[‡]Z.L.C. and X.Y.Z. contributed equally to this work

Summary

Fungal-mineral interactions can produce large amounts of biogenic nano-size (~1–100 nm) minerals, yet their influence on fungal physiology and growth remains largely unexplored. Using *Trichoderma guizhouense* NJAU4742 and magnetite (Mt) as a model fungus and mineral system, we have shown for the first time that biogenic Mt nanoparticles formed during fungal-mineral cultivation exhibit intrinsic peroxidase-like activity. Specifically, the average peroxidase-like activity of Mt nanoparticles after 72 h cultivation was ~2.4 times higher than that of the original Mt. Evidence from high resolution X-ray photoelectron spectroscopy analyses indicated that the unique properties of magnetite nanoparticles largely stemmed from their high proportion of surface non-lattice oxygen, through occupying surface oxygen-vacant sites, rather than Fe redox chemistry, which challenges conventional Fenton reaction theories that assume iron to be the sole redox-active centre. Nanoscale secondary ion mass spectrometry with a resolution down to 50 nm demonstrated that a thin (<1 μm) oxygen-film was present on the surface of fungal hyphae. Furthermore, synchrotron radiation-based micro-FTIR spectra revealed that surface oxygen groups corresponded mainly to organic OH, mineral OH, and carbonyl groups. Together, these findings highlight an important, but unrecognized, catalytic activity of mineral nanoparticles produced by fungal-mineral interactions and contribute substantially to our understanding of mineral

nanoparticles in natural ecosystems.

Introduction

Fungi-mineral interactions not only play essential roles in rhizospheric organic matter degradation and phosphorus cycling (Smits *et al.*, 2009; Loron *et al.*, 2019), but they also drive the biogeochemical cycling of other elements (Jongmans *et al.*, 1997; Lloyd *et al.*, 2008; van Schöll *et al.*, 2008). During fungal-mineral interactions, large amounts of novel biogenic nanoscale (~1–100 nm) minerals can be produced (Adeyemi and Gadd, 2005; Petkov *et al.*, 2009; Fomina *et al.*, 2010), including nanominerals and mineral nanoparticles (Hochella et al., 2008). The former are defined as minerals that only exist in the nano-size range (e.g., ferrihydrite and allophane), while the latter refers to minerals that can also exist in larger sizes (Hochella *et al.*, 2008). These microbially derived nanoscale minerals have properties that are distinct from those of bulk mineral phases, and can play an important role in binding and storing soil organic carbon and other elements (Yu *et al.*, 2017; Kramer and Chadwick, 2018). However, their influence on fungal physiology and growth remains largely unexplored.

Among these nano-size minerals, redox-active iron (Fe) nanoparticles have been shown to possess intrinsic peroxidase-like activity (so-called nanozymes) in acidic environments (Gao *et al.*, 2007; Chen *et al.*, 2012). Specifically, they can affect reactive oxygen species (ROS), including superoxide ($O_2^{\bullet-}$), hydrogen peroxide (H_2O_2) and hydroxyl radicals ($HO^{\bullet}$), in biological systems (Chen *et al.*, 2012; Wang *et al.*, 2017).

Because ROS are widespread (Diaz *et al.*, 2013), these nano-size minerals are beneficial for biological systems in terms of nutrient acquisition (Op De Beeck *et al.*, 2018). However, the catalytic mechanisms through which biogenic nano-size minerals act as nanozymes in biological systems are poorly understood (Wei and Wang, 2013; Huang *et al.*, 2019).

Recent studies have shown that the catalytic activity of biogenic iron minerals may be attributable to the chemistry of either Fe (Melton *et al.*, 2014; Du *et al.*, 2019; Yu *et al.*, 2019) or surface oxygen anions (Mueller *et al.*, 2015; Li *et al.*, 2019; Wang *et al.*, 2019). Iron is the fourth most abundant element in the Earth's crust and occurs primarily as the ferrous [Fe(II)] or ferric [Fe(III)] forms (Melton *et al.*, 2014; Kappler *et al.*, 2015; Winkler *et al.*, 2018). In the presence of $O_2^{\bullet-}$ and H_2O_2, the Fe(II) ion or Fe(III)-containing minerals can act as catalysts to promote Fenton or Fenton-like reactions, respectively (Melton *et al.*, 2014; Yuan *et al.*, 2018; Yu *et al.*, 2019; Han *et al.*, 2020). Compared to the Fenton reaction, which operates only under a limited range of acidic conditions, Fenton-like reactions are common in natural systems because they can operate over a wide range of pH values (Pereira *et al.*, 2012; Yu *et al.*, 2020). Furthermore, the catalytic centres that have been proposed to occur on nanoparticle surfaces are ~50-fold more effective for HO$^{\bullet}$ production than dissolved Fe(III) (Voinov *et al.*, 2011). Therefore, it seems that both surface oxygen structures (Mueller *et al.*,

2015; Li *et al.*, 2019; Wang *et al.*, 2019) and Fe chemistry (Gao *et al.*, 2007; Garrido-Ramírez *et al.*, 2010; Han *et al.*, 2020) play important roles in controlling the catalytic activity of these iron oxides. However, very few studies have addressed the underlying catalytic mechanisms of biogenic nano-size minerals that may possess distinctly different properties from those of synthetic minerals, because of their surface modification by biomolecules (Liu and Liu, 2017) or unique hierarchical structures (Yang *et al.*, 2020).

The objectives of this study were (i) to test whether fungal-derived iron minerals possess peroxidase-like activity, and (ii) to explore the catalytic mechanisms of fungal-derived iron minerals. For these purposes, we used *Trichoderma guizhouense* NJAU4742 and magnetite (Mt) as a model fungus and mineral system, due to their ubiquity in a wide range of environments (You *et al.*, 2019; Yu *et al.*, 2019; Lin *et al.*, 2020). Throughout our experiments, results from standardized assays of peroxidase nanozymes and the advanced techniques of high resolution X-ray photoelectron spectroscopy (XPS), high performance liquid chromatography (HPLC), nanoscale secondary ion mass spectrometry (NanoSIMS) and synchrotron radiation-based micro-FTIR (μ-FTIR) were integrated to identify the specific catalytic mechanisms that operate in these fungal-derived iron minerals. Our results showed that biogenic Mt nanoparticles formed during fungal-mineral cultivation exhibit intrinsic peroxidase-like

activity. Furthermore, we found that, the electronic structure, especially that of surface oxygen anions, controlled the catalytic activity of nanozymes via occupying surface oxygen-vacant sites, which challenges the scope of conventional Fenton reaction theories that assume iron to be the sole redox-active centre.

Results

Changes in pH, iron oxidation state and particle size during fungal-mineral cultivation

During cultivation of the fungal-mineral combination or growth of the fungus alone, the media pH values dropped from pH 5.2 to 2.2 over the initial 72 h and then stabilized, whereas in the mineral alone cultivation they remained constant at pH 5.2 (Fig. 1a). To further support the observed pH changes, the local pH values of hyphae in the *T.* + Mt treatment were determined using the fluorescent molecular probe SNARF4F and confocal laser scanning microscopy observations (Supporting Information Fig. S1). Calibration of the signals indicated pH values ranging from pH 4.5 to 6.1 in the local environment near the hyphae, suggesting a weak acidic pH for the Mt-derived fungal samples (Supporting Information Fig. S1). By adding HEPES buffer (i.e., initial pH of 7.0) into the *T.* + Mt cultivation media, the decline in media pH values was found to be dependent on the concentration of glucose, i.e., slightly (~0.3 pH units) under a low

concentration (2 g/L) but markedly (~3 pH units) under a high concentration (10 or 20 g/L).

Along with the pH decrease, there was an increase in dissolved Fe, dissolved Fe(II), total Fe(II) and structural Fe(II) in the *T.* + Mt treatment (Fig. 1b-e and Supporting Information Table S1). However, the control treatment in which minerals were incorporated in the medium without fungal inoculation did not show any release of dissolved Fe or Fe(II), suggesting that the growth of *T. guizhouense* altered the medium pH by excreting organic acids and/or protons (H$^+$) therefore playing a role in the release and/or reduction of Fe. Furthermore, results from the pH control treatment (i.e., controlling a pH of ~2.2 by adding HCl) provided direct evidence demonstrating that an increase in proton concentration (~1000 times) had more impact on an increase in iron dissolution (Fig. 1b) and iron reactivity (Fig. 1c-e) than the decrease in particle size (Fig. 1f and Supporting Information Fig. S2). The reduction of the glucose concentration in the medium could also result in a decrease in iron dissolution (Fig. 1b) and iron reactivity (Fig. 1c-e) as well as an increase in particle size (Fig. 1f), owing to a possible decline in excretion of organic acids or protons (H$^+$). During fungal-mineral cultivation, the particle size of the iron oxide in solution gradually decreased up to 10-fold over the initial 48 h from ~215 nm to ~20 nm (Fig. 1f and Supporting Information Fig. S2). However, after release of particles from fungal aggregates using ultrasound

treatment (20 kHz, 120 W, 10 min), this decreased ~2-fold over 120 h from ~215 nm to ~105 nm (Supporting Information Fig. S3 and S4). Therefore, changes in particle size were driven by not only reductive dissolution (Fig. 1b-e) but also fungal entanglement and aggregation which embedded a considerable amount of bulk Mt particles into such aggregates (Supporting Information Fig. S5).

To further examine the effect of fungal-mineral interaction on the morphology and mineralogy of Mt, transmission electron microscopy (TEM) and X-ray diffraction (XRD) analyses were used. Although the morphology of Mt at the edge of mineral particles was blurred, some small particles were evident at the edge of the minerals after 120 h cultivation (Supporting Information Fig. S6). XRD patterns showed no evidence for the formation of any new mineral phases (Supporting Information Fig. S7).

Peroxidase-like nanozyme activity of Mt nanoparticles during fungal-mineral cultivation

To assess the peroxidase-like nanozyme activity of Mt nanoparticles during fungal-mineral cultivation, we used the classic colour reaction of 3,3',5,5'-tetramethylbenzidine (TMB). During fungal-mineral cultivation, peroxidase-like

nanozyme activity increased rapidly over the initial 72 h and then approached a plateau until 120 h (Figs. 2 and 3a). Specifically, the average peroxidase-like activity (~0.029 units) of Mt nanoparticles after 72 h cultivation with *T. guizhouense* was ~2.4 times higher than that of the original Mt (~0.012 units).

Along with increased peroxidase-like activity, the generation of HO$^\bullet$ in the media of the fungal-Mt system was ~30–50% higher than that from the fungus alone (Fig. 3b), and the shape of the curve for the fungus-mineral cultivation system suggested that small Mt particles (Fig. 1d and Supporting Information Figs. S2-S4) were more efficient than large Mt particles for the catalytic breakdown of H_2O_2 to HO$^\bullet$. In contrast, HO$^\bullet$ was not detected in the Mt alone culture media (Fig. 3b). To further eliminate the effects of other factors (e.g., enzymes, secondary metabolites in the culture filtrate) on HO$^\bullet$ production, the extracted Mt particles (1%) from the *T.* + Mt treatment were directly incubated with H_2O_2 (5 µM) in the presence of TPA (2.5 mM) for 2 h (Fig. 3c). The results showed that the iron oxides reduced by the fungus resulted in increased HO$^\bullet$ production after 48 h cultivation and the HO$^\bullet$ production of Mt particles at 120 h was approximately 2.3 times higher than that of raw Mt particles. Note that HO$^\bullet$ production at 120 h in the extracted Mt (Fig. 3c) was lower (~15%) than that in the whole samples (Fig. 3b), suggesting that the Mt minerals are not the sole possible source of H_2O_2 splitting and that other components in the culture filtrate (e.g., enzymes, secondary

metabolites) may also contribute a proportion of total HO$^{\bullet}$ production. Except for 120 h, the HTPA concentration in Fig. 3c was higher than that in Fig. 3b, because of the use of a higher H_2O_2 concentration in Fig. 3c than in Fig. 3b. There was a positive correlation between peroxidase-like activity and HO$^{\bullet}$ production over the initial 72 h cultivation. However, after 72 h, HO$^{\bullet}$ production seemed to be independent of peroxidase-like activity (Fig. 3d). This independence of HO$^{\bullet}$ production from peroxidase-like activity may suggest recycling of redox-active compounds, e.g., enzymes and/or secondary metabolites produced by the fungus.

Fe 2p and O 1s XPS spectra of Mt nanoparticles before and after fungal-mineral cultivation

To identify the composition and oxidation state of elements on or near the surface (2–10 nm) of minerals, high resolution XPS was used to examine the Mt before and after 120 h cultivation. In the Fe 2p XPS spectra, the Fe $2p_{3/2}$ peak was similar for the Mt before and after 120 h cultivation (Supporting Information Fig. S8), and curve-fitting demonstrated that both Fe(II) and Fe(III) were present in the Mt before and after 120 h fungus cultivation. However, the surface Fe(II)/Fe(III) ratio increased from ~12% in the original Mt to ~22% of Mt after 120 h fungus cultivation (Fig. 4a,c and Supporting

Information Table S2). Similarly, the Fe(II)/Fe(III) ratio increased from 0.26 (i.e., ~21%) in the original Mt to 0.74 (~42%) of total Fe and 0.59 (~37%) of structural Fe after 120 h cultivation (Supporting Information Table S1), which was higher than the surface Fe(II)/Fe(III) ratio (Supporting Information Table S2), owing to Mt containing a considerable amount of inherent Fe(II). In addition, O=C-O bonds on the hematite decreased from 15.5% to 9.5%, suggesting that high energy bonds may be sacrificed to rejuvenate surface Fe(II) (Supporting Information Fig. S9).

In stark contrast to the small change observed with the Fe 2p XPS spectra, the O 1s XPS spectra of Mt (Fig. 4b,d) showed a ~3-fold intensity increase at ~532 eV and a concomitant decrease at ~530 eV as a result of fungal cultivation; at the same time there was a large increase in the generation of HO$^\bullet$ (Fig. 3b, Supporting Information Table S3). Thus, there was a shift in the position of this peak from 531.1 to 532.6 eV as a result of cultivation of the Mt with *T. guizhouense* (Supporting Information Table S3). Electron paramagnetic resonance (EPR) was also used to investigate the Mt samples, but the spectra were very broad as a result of the extended magnetically ordered structure and no marked features from singly ionized oxygen vacancies (Vo$^+$) could be specifically identified. Nevertheless, changes in the lineshape were observed as a function of incubation time with the fungus, thus indicating that some changes were introduced in the magnetic properties of the mineral.

Spatial distribution of Fe, O and organic components during fungal-mineral cultivation

To further explore the spatial distribution of *T. guizhouense* and Mt during fungal-mineral cultivation, correlative scanning electronic microscopy (SEM) and NanoSIMS images were first applied to observe the distribution of Fe, O and CN *in situ* (Fig. 5 and Supporting Information Fig. S11). After 120 h cultivation, *T. guizhouense* became entangled with Mt, suggesting a close contact between the fungus and the mineral (Fig. 5a and Supporting Information Fig. S11). The NanoSIMS images of $^{12}C^{14}N^-$, $^{16}O^-$, and $^{56}Fe^{16}O^-$ ion masses showed the submicron elemental distribution and spatial heterogeneity in the fungal-mineral interactions (Fig. 5b–d and Supporting Information Fig. S5). The colour bar on the NanoSIMS images (Fig. 5b–d and Supporting Information Fig. S11), from blue to red, directly showed the ion masses intensity from relatively weak to strong at a spatial and submicron scale. The NanoSIMS images (Fig. 5b–d and Supporting Information Fig. S11) indicated that the minerals and fungal derived organic materials were highly heterogeneous. Furthermore, our composite NanoSIMS images demonstrated that the arrangement and intensity obviously varied between the $^{12}C^{14}N^-$, $^{16}O^-$, and $^{56}Fe^{16}O^-$ ion masses (Fig. 5e–g and Supporting Information Fig. S11). Interestingly, high resolution (down to 50 nm) NanoSIMS

images revealed that a thin-film (<1 μm thick) of $^{16}O^-$ (oxygen in Mt) rather than $^{56}Fe^{16}O^-$ (iron in Mt) was present on the surface of $^{12}C^{14}N^-$ (fungal biomass) (Fig. 5e,g and Supporting Information Fig. S11), suggesting that fungal activities altered the distribution of Fe and O in the surface regions of the mineral owing to the reduction and release of Fe.

Next, spatially-related μ-FTIR was used to identify the distribution of *T. guizhouense* and Mt at the functional group level. A stack of μ-FTIR spectra, with a distance of 0 μm indicating the start point of the red arrow in Fig. 6a, are presented in three-dimensional (3D) or two-dimensional (2D) modes in Fig. 6b and 6c, respectively. The fungus and mineral were differentiated by their unique functional groups. Consistent with the observations derived from NanoSIMS images, spatially-related μ-FTIR spectra also revealed that functional groups associated with the iron mineral, i.e., Fe-OH (3450 cm^{-1}) and Fe-O (860 cm^{-1}) (Sun *et al.*, 2017; Yu *et al.*, 2019), were distributed on the surface (with ~5–7 μm thickness) of the fungal-mineral samples (Fig. 6). In contrast, fungal produced organic functional groups, e.g., lipid (C-H, 2850 cm^{-1} and 2920 cm^{-1}), carbonyl (C=O, 1738 cm^{-1}), amide I (C=O, 1650 cm^{-1}), amide II (N-H, 1540 cm^{-1}), and carbohydrate (OH, 1180 cm^{-1}), were mainly distributed in the interior of the fungal-mineral samples. Compared to cultivation of the fungus alone (Supporting Information Fig. S12), fungal-mineral cultivation dramatically increased

the absorbance of bands from extracellular lipids (2850 cm^{-1} and 2920 cm^{-1}) and proteins (1650 cm^{-1} and 1540 cm^{-1}) (Fig. 5g,h). In addition, spatially-related μ-FTIR spectra showed the presence of stretching vibrations for phosphates (1400–1000 cm^{-1}) on the fungal-mineral samples (Fig. 6) but not those from cultivation of *T. guizhouense* alone (Supporting Information Fig. S12). Interestingly, the distribution pattern of phosphates was similar to that of iron oxides (Fe-O, 860 cm^{-1}), suggesting that phosphates were adsorbed onto the nanoparticles.

Discussion

Fungi excrete extracellular $O_2^{\bullet-}$ and H_2O_2, which are involved in nutrient acquisition via extracellular Fenton chemistry (Op De Beeck *et al.*, 2018). In the presence of iron (oxyhydr)oxides, high concentrations of hydroxyl radicals were produced and showed a similar trend as with iron oxides (Yu *et al.*, 2019). In this study, we have demonstrated for the first time that fungal produced Mt nanoparticles exhibited a higher peroxidase-like activity than the original Mt (Figs. 2,3a).

The increased peroxidase-like activity may be attributable to an increase in enzyme-like activity of the smaller Mt particles (Gao *et al.*, 2007; Chen *et al.*, 2012) or the sorption behaviour of Mt particles for enzymes and/or secondary metabolites (Wu

et al., 2014). Mt particles have been shown to possess intrinsic peroxidase-like activity in acidic environments (Gao *et al.*, 2007; Chen *et al.*, 2012). In soil, Allison (2006) found that although gamma irradiation killed soil microorganisms, gamma-irradiated soil retained 35–70% of the enzyme activity throughout a 21-day incubation period, pointing to the possibility of minerals processing intrinsic enzyme-like activity. In addition, Wu *et al.* (2014) showed that, compared to the free enzyme, mineral-adsorbed enzymes exhibited increased catalytic activities at low pH, implying the possible contribution of minerals to catalytic activity by acting through an intrinsic enzyme-like mechanism. Moreover, mineral-initiated catalytic reactions occurring at hyphal-mineral interfaces may facilitate microbial iron uptake (Fig. 5h) and thus fungal growth (Yu *et al.*, 2019), which is analogous to observations of a melting glacier in providing bioavailable Fe (Hawkings *et al.*, 2014, 2018). Iron solubilization for fungal utilization can be driven by both fungal excretion of H^+, organic acids, siderophores, and bioreduction reactions, as for other metals (Gadd, 2007, 2010; Smits *et al.*, 2009; Yu *et al.*, 2019). Siderophores are important in iron-limited conditions and where soluble Fe(II) is available may not be required. Proton- and ligand-mediated solubilization mechanisms are likely to be of high importance, especially the role of organic acids (Gadd, 1999, 2007; Kirtzel *et al*., 2020). Many geoactive fungi produce a range of organic acids depending on environmental and nutritional conditions and these can

underpin mineral and metal transformations (Gadd, 1999, 2007; Wei *et al.*, 2012; Kirtzel *et al.*, 2020). Organic acids that are produced by *Trichoderma harzianum* include oxalic acid, citric acid, D_L-malic acid, succinic acid, and fumaric acid (Altomare *et al.*, 1999). It is noteworthy that oxalate can also act as a metal reductant (Gadd, 1999; Wei et al., 2012).

Apart from Mt nanoparticles, other chemical synthetic iron (oxyhydr)oxide nanoparticles, e.g., ferromagnetic nanoparticles, have been shown to catalyze H_2O_2 breakdown and produce $HO^{\bullet}$ through a peroxidase-like reaction in acidic environments (Gao *et al.*, 2007; Chen *et al.*, 2012). In general, synthetic iron (oxyhydr)oxide nanoparticles have a relatively homogeneous particle size (Chen *et al.*, 2012; Huang *et al.*, 2019). In contrast, biogenic iron (oxyhydr)oxide nanoparticles often possess hierarchical structures that show superior catalytic activity due to the built-in electric field and the high proportion of interfacial elements (Yao *et al.*, 2017; Yang *et al.*, 2020). Interestingly, our NanoSIMS and TEM observation suggested the presence of hierarchical structures after 120 h cultivation (Fig. 5 and Supporting Information Fig. S6), which is similar to observations in a previous report (Yang *et al.*, 2020). These hierarchical structures may be caused by proton-promoted reactions, initiated by fungal excretion of H^+ and organic acids (Yu *et al.*, 2019), followed by reduction and/or
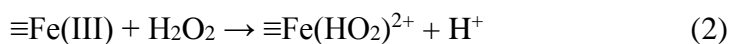
complexation of Fe atoms by organic molecules produced by the fungus, finally resulting in destruction of the mineral structure (Furrer, 1986).
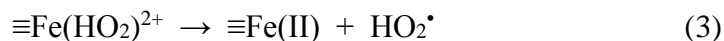
Nanozyme mimetic catalysis reactions occur mainly at the nanoparticle surface (Liu and Liu, 2017). XPS can be used to identify the composition and oxidation state of elements on or near the surface (2–10 nm) of minerals (Grosvenor *et al.*, 2004; Yamashita and Hayes, 2008), and provide insights into the catalytic mechanisms involved. Fe(II) is more efficient than Fe(III) in catalyzing the production of HO$^{\bullet}$ from H_2O_2 (Chen *et al.*, 2012; Trusiak *et al.*, 2018), and increasing the proportion of Fe(II) can effectively enhance the peroxidase-like activity of minerals (Gao *et al.*, 2007). However, the small increase in surface Fe(II) (Fig. 4a,c) suggested that increasing the amount of surface Fe(II) was not be the dominant catalytic mechanism of Mt.

To further elucidate the catalytic mechanisms of Mt nanoparticles, we examined surface oxygen chemistry of the Mt nanoparticles using O 1s XPS spectra (Fig. 4b,d). Note that the peaks at 530 eV and 532 eV are assigned to lattice oxygen (O_L, O^{2-}) and non-lattice oxygen (O_{NL}) (Li *et al.*, 2019). The O_{NL} may be attributed to adsorbed O species, including OH^-, C–O, and O–C=O (Li *et al.*, 2019). O 1s XPS spectra (Fig. 4b,d) indicated that in the original Mt, O_L was the dominant oxygen component, but the sample cultivated with the fungus increased the contribution from adsorbed O species

(OH⁻, C–O, O–C=O). It is proposed that these adsorbed O species occupy surface oxygen-vacant sites (i.e., V_O) and thus facilitate the catalytic process (Nagarajan *et al.*, 2008; Yang *et al.*, 2013; Li *et al.*, 2019). The V_O consists of V_O^+, doubly ionized Vo (V_O^{+2}), and neutral Vo (V_O^0). Of these, only V_O^+ is paramagnetic and potentially observable by EPR (Vanheusden *et al.*, 1996; Li *et al.*, 2019), but the extended magnetically ordered structure prevented its identification in our Mt samples, although changes in the surface composition could contribute to the changes in the spectra observed as a result of incubation of Mt with the fungus (Supporting Information Fig. S10).

The proposed catalytic mechanisms of fungus produced magnetite nanoparticles acting as nanozymes are shown in Fig. 7. The conventional view (Fig. 7a) is that iron acts as the sole redox-active centre. Fe redox chemistry, known as Fenton (equation 1) or Fenton-like reactions (equations 2–4), plays a considerable role in the catalytic reactions of Fe minerals (Garrido-Ramírez *et al.*, 2010; Huang *et al.*, 2016; Op De Beeck *et al.*, 2018; Yu *et al.*, 2019; Han *et al.*, 2020):

$$Fe(II) + H_2O_2 \rightarrow Fe(III) + OH^- + HO^\bullet \qquad (1)$$

$$\equiv Fe(III) + H_2O_2 \rightarrow \equiv Fe(HO_2)^{2+} + H^+ \qquad (2)$$

$$\equiv Fe(HO_2)^{2+} \rightarrow \equiv Fe(II) + HO_2^{\bullet} \tag{3}$$

$$\equiv Fe(II) + H_2O_2 \rightarrow Fe(III) + OH^- + HO^{\bullet} \tag{4}$$

where $\equiv Fe$ represents the surface iron. In addition, the produced $O_2^{\bullet-}$ may also react with H_2O_2, in what is known as the Haber−Weiss reaction (equation 5) (Haber and Weiss, 1934). This reaction could also contribute to $HO^{\bullet}$ generation (Hayyan *et al.*, 2016).

$$H_2O_2 + O_2^{\bullet-} \rightarrow OH^- + O_2 + HO^{\bullet} \tag{5}$$

However, our current XPS results (Fig. 4) provide direct evidence for a major role of surface oxygen chemistry in controlling the peroxidase-mimicking activity of the Mt nanoparticles. Therefore, the alternative mechanism proposed here (Fig. 7b) considers the contribution of both Fe and O to the catalytic activity of Mt nanoparticles, and highlights that surface oxygen anions play a major role in controlling the catalytic activity of the iron nanoparticles. Previous research has also shown that electrons can be transferred from the support to Fe(III) on the Mt surface through O_{NL} bonds, thereby regenerating surface Fe(II) (Adhikari *et al.*, 2017; Zeng *et al.*, 2020), which may contribute to the mitigation of surface deactivation and promote $HO^{\bullet}$ production. Furthermore, since the single O–O bond in H_2O_2 is much weaker than the O–O double

bond in O_2, back-donation of localized electrons after the adsorption of H_2O_2 on O_{NL} seems to induce the catalytic dissociation of H_2O_2 to generate $HO^\bullet$ (Li *et al.*, 2017). The association of Vo^+ with the splitting of H_2O_2 is the result of it being occupied by adsorbed adventitious O species (e.g., OH^-) (Li *et al.*, 2019; Wang *et al.*, 2019). The hydroxylated surface inevitably benefits the following reactions (equations 6 and 7) and increases the yield of $HO^\bullet$.

$$Vo^+ + e^- = Vo \tag{6}$$

$$Vo\,(h^+) + OH^- = HO^\bullet \tag{7}$$

Thus, the peroxidase-like catalytic activity of the Fe-bearing nanoparticles may reside in the presence of Vo that can serve as electron acceptors and donors to facilitate charge transfer in H_2O_2 (Li *et al.*, 2017):

This catalytic mechanism highlights the importance of the electronic structure, especially that of surface oxygen anions, for nanozymes in controlling their catalytic activity, which is beyond the scope of conventional Fenton reaction theories that assume iron to be the sole redox-active centre (Jensen *et al.*, 2001; Pereira *et al.*, 2012; Sekar and DiChristina, 2014). In addition, the adsorption of phosphates onto the nanoparticles may potentially affect the production of enzymes and/or secondary metabolites to

release this adsorbed phosphate (e.g., through reductive dissolution), affecting the production of HO$^{\bullet}$ and therefore the conclusions of the presented work. Future research could test the catalytic mechanism by examining the effects of Mt nanoparticles having distinct oxygen vacancies (Wang *et al.*, 2019) on H_2O_2 consumption and hydroxyl radical generation. The μ-FTIR spectra (Fig. 6) further revealed that surface oxygen groups, occupying Vo sites, comprised mainly organic OH (3295 cm^{-1}) (Yu *et al.*, 2019), mineral OH (3450 cm^{-1}) (Yu *et al.*, 2019), and carbonyl (C=O, 1738 cm^{-1}) groups (Bonneville *et al.*, 2020).

Nanomaterials have recently been found to exhibit enzyme-like catalytic activities that have been utilized for immunoassays, biosensing, and cancer diagnosis (Gao *et al.*, 2007; Chen *et al.*, 2012; Wei and Wang, 2013). This is, to our knowledge, the first report of fungal produced magnetite nanoparticles possessing intrinsic nanozyme-like activity, highlighting the unknown catalytic activities of mineral nanoparticles to microbes. These unique properties of magnetite nanoparticles were further revealed to stem largely from the high proportion of surface non-lattice oxygen atoms (Fig. 4) that may occupy surface oxygen-vacant sites (Nagarajan *et al.*, 2008; Yang *et al.*, 2013; Li *et al.*, 2019). Firstly, fungal-derived surface non-lattice oxygen atoms in the mineral nanoparticles affect the production of HO$^{\bullet}$ in the extracellular environment. Therefore, mineral nanoparticles acting as nanozymes can affect fungal growth, and the formation

of HO$^{\bullet}$ may expedite the breakdown of recalcitrant soil organic matter, such as lignocellulosic residues, and facilitate nutrient acquisition in nutrition-poor environments (Shah *et al.*, 2016; Op De Beeck *et al.*, 2018). Secondly, the formation of HO$^{\bullet}$ derived from non-lattice oxygen atoms in the mineral nanoparticles may play an important role in the attenuation of contaminants in the local fungal environment (Sekar and DiChristina, 2014; Gu *et al.*, 2016).

More broadly, the Earth has several thousands of terragrams (Tg) of natural nanoparticles moving around the planet annually (Hochella *et al.*, 2019). Since the intrinsic peroxidase activity of iron nanoparticles was first reported in 2007, more than 300 types of nanomaterials have been reported to possess enzyme-like catalytic activities (Jiang *et al.*, 2018; Zhang *et al.*, 2020). Therefore, the utilization of mineral nanoparticles as nanozymes by microorganisms may be ubiquitous. Given the ubiquity of nanomaterials (Hochella *et al.*, 2019) and microorganisms (Fierer, 2017) on Earth, this study has prompted us to further explore the influences of mineral nanoparticles on microorganisms to improve our understanding of elemental cycles (e.g., carbon, nitrogen, and phosphorus) in a changing world.

Experimental procedures

Organism and growth conditions

For growth of *Trichoderma guizhouense* NJAU 4742, the following minimal medium was used (per liter Milli Q water): 0.1 g urea, 1.4 g $(NH_4)SO_4$, 1.5 g KH_2PO_4, 0.1 g $CaCl_2 \cdot 2H_2O$, 0.4 g $MgSO_4 \cdot 7H_2O$, 0.1 g yeast extract, 5 mg $FeSO_4 \cdot 7H_2O$, 5 mg $CoCl_2$, 1.8 mg $MnSO_4 \cdot H_2O$, 2.5 mg $ZnSO_4 \cdot 7H_2O$, 20 g glucose, and 0.6 g NaCl (Zhang *et al.*, 2019). Magnetite was purchased from Sinopharm Chemical Reagent Cor., Ltd., Shanghai, China. Particle size distibution, TEM and XRD patterns of Mt are available as Supporting Information Figs. S1–S3 and Texts S1–S2, respectively. The liquid medium containing 1% (w/v) Mt was inoculated with *T. guizhouense* conidia (10^4 mL^{-1}) and incubated in a shaking incubator (170 rpm).

The following cultivations were conducted, including *T.* + Mt (*T. guizhouense* plus Mt), *T.* (*T.* alone), Mt (Mt alone), pH control (i.e., controlling a pH of ~2.2 by adding HCl), 2 G, 10 G and 20 G (i.e., the concentration of glucose in the medium being set to 2 g/L, 10 g/L and 20 g/L, respectively, and a pH of ~2.2 being controlled at ~7.0 by adding HEPES buffer). All cultivation experiments were conducted in triplicate and performed at 28°C in the dark.

Peroxidase-like nanozyme activity measurement

Peroxidase-like nanozyme activity assays were carried out in 2-mL tubes using 10 µL of 5 mg mL^{-1} 3,3',5,5'-tetramethylbenzidine (TMB) solution in DMSO as the substrate. Each tube contained one mL of test solution with 0.5 mg Mt in 0.2 M NaAc-HAc buffer (pH 3.6). A blue color was observed after H$_2$O$_2$ input (to a final concentration of 50 mM) at 28°C, and absorbance measurements were made at 652 nm every 15 s for up to 20 min. A sample without addition of H$_2$O$_2$ or TMB solution served as the control.

Nanozyme activity (units) were calculated as follows (equation 8) (Jiang *et al.*, 2018):

$$b_{nanozyme} = V/(\varepsilon \times l) \times (\Delta A / \Delta t) \tag{8}$$

where $b_{nanozyme}$ is the nanozyme activity expressed in catalytic units which are defined as the amount of nanozyme that produces 1 µmol of product per min at 28°C; V is the total volume of reaction solution (µL); ε is the molar absorption coefficient of the colorimetric substrate (typically maximized at 39000M^{-1} cm^{-1} at 652 nm for TMB); and l is the path length of light in the cuvette (cm). The quantity $\Delta A/\Delta t$ is the initial rate of change in absorbance at 652 nm in min^{-1}.

Quantification of HO•

Terephthalic acid (TPA, non-fluorescent) stock solution (Tokyo Chemical Industry Co Ltd, Tokyo, Japan) was added to samples to a final concentration of 2.5 mM, and after 2 h cultivation the fluorescent product from reaction with HO•, 2-hydroxyl TPA (HTPA), was quantified using an Agilent 1260 Infinity HPLC (Agilent Technologies Inc., Germany) system equipped with a Fluorescence Detector (G1321B) and a reverse-phase C18 column (Develosil ODS-UG5, 4.6 mm × 250 mm, Nomura Chemical Co., Japan). The concentration of HTPA was used as an estimate of the cumulative HO• generation (Li *et al.*, 2004). Mt nanoparticles were extracted at different cultivation times in the *T.* + Mt treatment using ultrasound (20 kHz, 120 W, 10 min) at 4 °C. The collected Mt particles were then lyophilized at −50 °C for 48 h. Finally, the extracted Mt nanoparticles were incubated with H_2O_2 (5 µM) in the presence of TPA (2.5 mM) for 2 h and the concentration of HTPA analyzed using HPLC.

High resolution XPS analyses

XPS data were collected using a PHI 5000 Versa Probe (UlVAC-PHI, Japan) spectrometer equipped with a monochromatic Al Kα X-ray source (1486.6 eV). The C

1s signal centered at 284.8 eV was used as an internal reference for the absolute binding energy (Du *et al.*, 2019). The surface charge induced by the photo ejection process was balanced using a flood gun at 6 eV. The base pressure in the spectrometer was 6.7×10^{-10} Torr. For wide-scan spectra, an energy range of 0–1100 eV was used with a pass energy of 80 eV and a step size of 1 eV. High-resolution scans were conducted according to the peak being examined with a pass energy of 40 eV and a step size of 0.06 eV. The energy precision of XPS was 0.06 eV. In order to investigate the oxidation state of surface (2–10 nm) sites, narrow scan spectra for Fe 2p3/2 were acquired. The high-resolution spectra of Fe 2p and O 1s regions were fitted using the CasaXPS software (Version 2.3.15) with a Shirley background and a Gaussian/Lorentzian line shape (Zhu *et al.*, 2014). Specifically, the background was adjusted with a High BE of 717 eV and a Low BE of 704 eV. The number of average Pts at end-points was None (i.e., 1 point). In addition, 20% was selected for the Gaussian/Lorentzian line shape.

NanoSIMS analysis

Fungal-mineral samples were dispersed in ethanol and dropped onto a silicon wafer, air-dried, and gold-coated. SEM (Zeiss EVO18) was performed with a 20-kV accelerating potential. NanoSIMS analyses were performed on a NanoSIMS 50L

instrument (Cameca, Gennevilliers, France) at the Institute of Geology and Geophysics, Chinese Academy of Sciences, Beijing, China. Prior to analysis, the gold coating layer (~10 nm) and possible contamination of the sample surface were pre-sputtered using a high primary beam current (Xiao *et al.*, 2016; Yu *et al.*, 2017). During the pre-sputtering, reactive Cs^+ ions were implanted into the sample to enhance secondary ion yields. Secondary ions $^{12}C^{14}N^-$, $^{16}O^-$ and $^{56}Fe^{16}O^-$ were collected simultaneously by electron multipliers with an electronic dead time of 44 ns. The presence of the $^{12}C^{14}N^-$ ion was interpreted as representing organic matter, while $^{16}O^-$ and $^{56}Fe^{16}O^-$ ions were interpreted as corresponding to minerals and Fe, respectively (Yu *et al.*, 2017; Newsome *et al.*, 2018). Although the fungus and the associated EPS matrix also contain oxygen, the $^{16}O^-$ yield is much greater in minerals than in organic matrices (Mueller *et al.*, 2012; Remusat *et al.*, 2012; Yu *et al.*, 2017). The charging effect resulting from nonconductive mineral particles was compensated through use of an electron flood gun. Composite multi-element images were constructed using Image J (version 1.45) with the OpenMIMS plugin (http://www.nrims.hms.harvard.edu/NRIMS_ImageJ.php).

Synchrotron radiation based μ-FTIR analysis

After 120 h cultivation, the hydrated cultivated samples from both fungal-mineral

interaction and fungal alone cultivation were frozen at −20 ℃ without embedding. Then, thin sections (1 µm in thickness) were cut on a cryomicrotome (Cyrotome E, Thermo Shandon Limited, UK) and transferred to infrared reflecting MirrIR Low-E microscope slides (Kevley Technologies, Ohio, USA).

Spatially-related µ-FTIR analysis was obtained at beamline BL01B1 of the National Center for Protein Science Shanghai (NCPSS). Spectra were recorded in reflectance mode using a Thermo Nicolet 6700 FTIR spectrometer and an infrared microscope with the following settings: aperture size 20×20 µm^2, step size 10×10 µm^2, resolution 4 cm^{-1}, spectral range 4000–650 cm^{-1} and 64 scans for mapping; aperture size 20 µm, step size 1×1 µm^2, resolution 4 cm^{-1}, spectral range 4000–650 cm^{-1} and 128 scans for stacking of µ-FTIR (Du *et al.*, 2019; Yu *et al.*, 2019). Both spectral mapping and the stacks of single FTIR spectra from µ-FTIR images was further processed using Omnic 9.0 software (Thermo Fisher Scientific Inc.) (Unger *et al.*, 2013). FTIR spectral background removal, normalization and automatic baseline correction were achieved using Omnic 9.0 software. The µ-FTIR data was processed by the RMieS-EMSC algorithm (v3) using MATLAB software (Bassan *et al.*, 2010).

Particle size and chemical analyses

The cultivated samples at the different time were filtered through a 0.45 µm pore size microfiltration membrane and then analyzed particle sizes in solution. Moreover, the cultivated samples (10 mL) were treated using ultrasound (20 kHz, 120 W, 10 min) at 4 °C and then collected the released Mt particles. The collected Mt particles were lyophilized at −50 °C for 48 h and 1 mg of Mt particles were added to 5 mL ethyl alcohol and stirred well. The sample was then filtered through a 0.45 µm pore size microfiltration membrane and this fraction of particles was the total Mt particles. The particle size was measured with a Zetasizer Nano-ZS (Malvern Panalytical, UK) using the following parameter settings: runs 3 times, temperature 25°C, liquid ethyl alcohol, angle 90°, run duration 2 min.

For chemical analyses, fungus-mineral samples were also first filtered through 0.45 µm filters. The filtrate (5 mL) was used to determine dissolved Fe by inductively coupled plasma-atomic emission spectroscopy (710/715 ICP-AES, Agilent, Australia). The solution pH was determined using a Mettler-Toledo acidimeter. The concentration of Fe(II) and Fe(III) was then measured by the 1,10-o-phenanthroline analytical method at 510 nm using a SpectraMax M5 spectrophotometer (Molecular Devices, Sunnyvale, CA, USA) (Wen *et al.*, 2018). Briefly, 1 mL of the samples was added to 4 mL of 0.5 M HCl and extracted for 24 h. The mixture was centrifuged and the supernatants were collected for determination of total Fe(II). For the analysis of the dissolved Fe(II), 1 mL

of the samples was taken and centrifuged to obtain the supernatants. Total extractable Fe was analyzed by the same procedure (*o*-phenanthroline colorimetric method) with the exception that the extractant was 1.5 M hydroxylamine hydrochloride as the extractant. The amount of hydroxylamine reducible Fe(III) was calculated as the difference between total extractable Fe and Fe(II). Structural Fe(II) included both sorbed Fe(II) and particulate Fe(II), and its concentration was obtained by subtracting dissolved Fe(II) from total Fe(II). Structural Fe(III) was calculated by subtracting dissolved Fe(III) from total Fe(III).

Competing financial interests: The authors declare no conflicts of interest.

References

Adeyemi, A. O., and Gadd, G. M. (2005) Fungal degradation of calcium-, lead- and silicon-bearing minerals. *Biometals* **18**: 269–281.

Adhikari, D., Zhao, Q., Das, K., Mejia, J., Huang, R., Wang, X., *et al*. (2017) Dynamics of ferrihydrite-bound organic carbon during microbial Fe reduction. *Geochim Cosmochim Acta* **212**: 212–233.

Allard, Th., Balan, E., Calas, G., Fourdrin, C., Morichon, E., and Sorieul, S. (2012). Radiation-induced defects in clay minerals: A review. *Nucl Instru Methods Phys Res B*, **277**, 112-120.

Allison, S. D. (2006) Soil minerals and humic acids alter enzyme stability: Implications for ecosystem processes. *Biogeochemistry* **81**: 361–373.

Altomare, C., Norvell, W. A., Björkman, T., and Harman, G. E. (1999) Solubilization of phosphates and micronutrients by the plant-growth-promoting and biocontrol fungus *Trichoderma harzianum* Rifai 1295-22. *Appl Environ Microbiol* **65**: 2926–2933.

Bassan, P., Kohler, A., Martens, H., Lee, J., Byrne, H. J., Dumas, P., *et al*. (2010) Resonant Mie Scattering (RMieS) correction of infrared spectra from highly scattering biological samples. *Analyst* **135**: 268–277.

Bonneville, S., Delpomdor, F., Préat, A., Chevalie, C., Araki, T., Kazemian, M., *et al*. (2020) Molecular identification of fungi microfossils in a Neoproterozoic shale rock. *Sci Adv* **6**: eaax7599.

Bose, S., Hochella, M. F., Gorby, Y. A., Kennedy, D. W., McCready, D. E., Madden, A. S., *et al*. (2009) Bioreduction of hematite nanoparticles by the dissimilatory iron reducing bacterium *Shewanella oneidensis* MR-1. *Geochim Cosmochim Acta* **73**: 962–976.

Chen, Z., Yin, J.-J., Zhou Y.-T., Zhang Y., Song L., Song M., *et al*. (2012) Dual enzyme-like activities of iron oxide nanoparticles and their implication for diminishing cytotoxicity. *ACS Nano* **6**: 4001–4012.

Cowart, R. E. (2002) Reduction of iron by extracellular iron reductases: implications for microbial iron acquisition. *Arch Biochem Biophys* **400**: 273–281.

Diaz, J. M., Hansel, C. M., Voelker, B. M., Mendes, C. M., Andeer, P. F., and Zhang, T. (2013) Widespread production of extracellular superoxide by heterotrophic bacteria. *Science* **340**: 1223–1226.

Du, H. Y., Yu, G. H., Sun, F. S., Usman, M., Goodman, B. A., Ran, W., and Shen, Q. R. (2019) Iron minerals inhibit the growth of *Pseudomonas brassicacearum* J12 via a free-radical mechanism: implications for soil carbon storage. *Biogeosciences* **16**: 1433–1445.

Feigl, F. J., Fowler, W. B., and Yip, K. L. (1974). Oxygen vacancy model for the E_1' centre in SiO_2. *Solid State Commu* **14**, 225-229.

Fierer, N. (2017) Embracing the unknown: disentangling the complexities of the soil microbiome. *Nat Rev Microbiol* **15**: 579–590.

Fomina, M., Burford, E. P., Hillier, S., Kierans, M., and Gadd, G. M. (2010) Rock-building fungi. *Geomicrobiol J* **27**: 624–629.

Furrer, G. S. W. (1986) The coordination chemistry of weathering: I. Dissolution kinetics of δ-Al_2O_3 and BeO. *Geochim Cosmochim Acta* **50**: 1847–1860.

Gadd, G.M. (1999). Fungal production of citric and oxalic acid: importance in metal speciation, physiology and biogeochemical processes. *Adv Microb Physiol* **41**: 47–92.

Gadd, G.M. (2007) Geomycology: biogeochemical transformations of rocks, minerals, metals and radionuclides by fungi, bioweathering and bioremediation. *Mycol Res* **111**: 3–49.

Gadd, G. M. (2010) Metals, minerals and microbes: geomicrobiology and bioremediation. *Microbiology* **156**: 609–643.

Gadd, G. M., Bahri-Esfahani, J., Li, Q., Rhee, Y.J., Wei, Z., Fomina, M., Liang, X. (2014) Oxalate production by fungi: significance in geomycology, biodeterioration and bioremediation. *Fungal Biol Rev* **28**: 36–55.

Gao, L., Zhuang, J., Nie, L., Zhang, J., Zhang, Y., Gu, N., *et al*. (2007) Intrinsic peroxidase-like activity of ferromagnetic nanoparticles. *Nat Nanotechnol* **2**: 577–583.

Garrido-Ramírez, E. G., Theng, B. K. G., and Mora, M. L. (2010) Clays and oxide minerals as catalysts and nanocatalysts in Fenton-like reactions – a review. *Appl Clay Sci* **47**: 182–192.Gu, C., Wang, J., Liu, S., Liu, G., Lu, H., and Jin, R. (2016) Biogenic Fenton-like reaction involvement in cometabolic degradation of tetrabromobisphenol A by *Pseudomonas* sp. fz. *Environ Sci Technol* **50**: 9981–9989.

Grosvenor, A. P., Kobe, B. A., Biesinger, M. C., and McIntyre N. S. (2004) Investigation of multiplet splitting of Fe 2p XPS spectra and bonding in iron compounds. *Surf Interf Anal* **36**: 1564–1574.

Haber, F., Weiss, J. (1934) The catalytic decomposition of hydrogen peroxide by iron salts. *Proc R Soc London Ser A* **147**: 332–351.

Hawkings, J. R., Wadham, J. L., Tranter, M., Raiswell, R., Benning, L. G., Statham, P. J., *et al.* (2014) Ice sheets as a significant source of highly reactive nanoparticulate iron to the oceans. *Nat Commun* **5**: 3929.

Hawkings, J. R., Benning, L. G., Raiswell, R., Kaulich, B., Araki, T., Abyaneh, M., *et al.* (2018) Biolabile ferrous iron bearing nanoparticles in glacial sediments. *Earth Planet Sci Lett* **493**: 92–101.

Han, R., Lv, J., Huang, Z., Zhang, S., and Zhang, S. (2020) Pathway for the production

of hydroxyl radicals during the microbially mediated redox transformation of iron (oxyhydr)oxides. *Environ Sci Technol* **54**: 902–910.

Hayyan, M., Hashim, M. A., AlNashef, I. M. (2016) Superoxide ion: generation and chemical implications. *Chem Rev* **116**: 3029–3085.

Hochella, M. F. Jr., Lower, S. K., Maurice, P. A., Penn, R. L., Sahai, N., Sparks, D. L., and Twining, B. S. (2008) Nanominerals, mineral nanoparticles, and Earth systems. *Science* **319**: 1631–1635.

Hochella, M. F., Mogk, D. W., Ranville, J., Allen, I. C., Luther, G. W., Marr, L. C., *et al*. (2019) Natural, incidental, and engineered nanomaterials and their impacts on the Earth system. *Science* 363: eaau8299.

Huang, X., Hou, X., Zhao, J., and Zhang, L. (2016) Hematite facet confined ferrous ions as high efficient Fenton catalysts to degrade organic contaminants by lowering H_2O_2 decomposition energetic span. *Appl Cataly B: Environ* **181**: 127–137.

Huang, Y., Ren, J., and Qu, X. (2019) Nanozymes: classification, catalytic mechanisms, activity regulation, and applications. *Chem Rev* **119**: 4357–4412.

Jensen, K. A., Houtman, C. J., Ryan, Z. C., and Hammel, K. E. (2001) Pathways for extracellular Fenton chemistry in the brown rot basidiomycete *Gloeophyllum trabeum*. *Appl Environ Microbiol* **67**: 2705–2711.

Jiang, B., Duan, D., Gao, L., Zhou, M., Fan, K., Tang, Y., *et al*. (2018) Standardized assays for determining the catalytic activity and kinetics of peroxidase-like nanozymes. *Nat Protoc* **13**: 1506–1520.

Jongmans, A. G., van Breemen, N., Lundström, U., van Hees, P. A. W., Finlay, R. D., Srinivasan, M., *et al*. (1997) Rock-eating fungi. *Nature* **389**: 682–683.

Kappler, A., Emerson, D., Gralnick, J., Roden, E., and Muehe, E. M. (2015) Geomicrobiology of Iron, Ehrlich's Geomicrobiology, Sixth Edition. CRC Press, pp. 343–399.

Kirtzel, J., 1 Ueberschaar, N., Deckert-Gaudig, T., Krause, K., Deckert, V., Gadd, G.M. and Kothe, E. (2020) Organic acids, siderophores, enzymes and mechanical pressure for black slate bioweathering with the basidiomycete *Schizophyllum commune*. *Environ Microbiol* **22**: 1535–1546.

Kramer, M. G., and Chadwick, O. A. (2018) Climate-driven thresholds in reactive mineral retention of soil carbon at the global scale. *Nat Clim Chang* **8**: 1104–1108.

Li, H., Shang, J., Yang, Z., Shen, W., Ai, Z., and Zhang, L. (2017) Oxygen vacancy associated surface Fenton chemistry: surface structure dependent hydroxyl radicals generation and substrate dependent reactivity. *Environ Sci Technol* **51**: 5685−5694.

Li, L., Abe, Y., Nagasawa, Y., Kudo, R., Usui, N., Imai, K., *et al*. (2004) An HPLC assay of hydroxyl radicals by the hydroxylation reaction of terephthalic acid. *Biomed Chromatog* **18**: 470–474.

Li, Y., Li, Y., Xu, X., Ding, C., Chen, N., Ding, H., and Lu, A. (2019) Structural disorder

controlled oxygen vacancy and photocatalytic activity of spinel-type minerals: A case study of ZnFe$_2$O$_4$. *Chem Geol* **504**: 276–287.

Lin, W., Kirschvink, J. L., Paterson, G. A., Bazylinski, D. A., and Pan, Y. (2020) On the origin of microbial magnetoreception. *Nat Sci Rev* **7**: 472–479.

Liu, B., and Liu, J. (2017) Surface modification of nanozymes. *Nano Res* **10**: 1125–1148.

Lloyd, J. R., Pearce, C. I., Coker, V. S., Pattrick, R. A., van der Laan, G., Cutting, R., *et al*. (2008) Biomineralization: linking the fossil record to the production of high value functional materials. *Geobiology* **6**: 285–297.

Loron, C. C., Francois, C., Rainbird, R. H., Turner, E. C., Borensztajn, S., and Javaux, E. J. (2019) Early fungi from the Proterozoic era in Arctic Canada. *Nature* **570**: 232–235.

Melton, E. D., Swanner, E. D., Behrens, S., Schmidt, C., and Kappler, A. (2014) The interplay of microbially mediated and abiotic reactions in the biogeochemical Fe cycle. *Nat Rev Microbiol* **12**: 797–808.

Mueller, C. W., Kölbl, A., Hoeschen, C., Hillion, F., Heister, K., Herrmann, A. M., and Kögel-Knabner, I. (2012) Submicron scale imaging of soil organic matter dynamics using NanoSIMS – from single particles to intact aggregates. *Org Geochem* **42**: 1476–1488.

Mueller, D. N., Machala, M. L., Bluhm, H., and Chueh, W. C. (2015) Redox activity of surface oxygen anions in oxygen-deficient perovskite oxides during electrochemical reactions. *Nat Commun* **6**: 6097.

Nagarajan, L., De Souza, R. A., Samuelis, D., Valov, I., Borger, A., Janek, J., *et al*. (2008) A chemically driven insulator-metal transition in non-stoichiometric and amorphous gallium oxide. *Nat Mater* **7**: 391–398.

Newsome, L., Lopez Adams, R., Downie, H. F., Moore, K. L., and Lloyd, J. R. (2018) NanoSIMS imaging of extracellular electron transport processes during microbial iron(III) reduction. *FEMS Microbiol Ecol* **94**: 5033680.

Op De Beeck, M., Troein, C., Peterson, C., Persson, P., and Tunlid, A. (2018) Fenton reaction facilitates organic nitrogen acquisition by an ectomycorrhizal fungus. *New Phytol* **218**: 335–343.

Pereira, M. C., Oliveira, L. C. A., and Murad, E. (2012) Iron oxide catalysts: Fenton and Fentonlike reactions – a review. *Clay Miner* **47**: 285–302.

Petkov, V, Ren, Y, Saratovsky, I, Pastén, P., Gurr, S. J., Hayward, M. A., *et al*. (2009) Atomic-scale structure of biogenic materials by total X-ray diffraction: a study of bacterial and fungal MnO$_x$. *ACS Nano* **3**: 441–445.

Remusat, L., Hatton, P. J., Nico, P. S., Zeller, B., Kleber, M., and Derrien, D. (2012) NanoSIMS study of organic matter associated with soil aggregates: advantages, limitations, and combination with STXM. *Environ Sci Technol* **46**: 3943−3949.

Sekar, R., and DiChristina, T. J. (2014) Microbially driven Fenton reaction for degradation of the widespread environmental contaminant 1,4-dioxane. *Environ Sci Technol* **48**: 12858–12867.

Shah, F., Nicolás, C., Bentzer, J., Ellström, M., Smits, M., Rineau, F., *et al*. (2016) Ectomycorrhizal fungi decompose soil organic matter using oxidative mechanisms adapted from saprotrophic ancestors. *New Phytol* **209**: 1705–1719.

Smits, M. M., Herrmann, A. M., Duane, M., Duckworth, O. W., Bonneville, S., Benning, L. G., and Lundström, U. (2009) The fungal–mineral interface: challenges and considerations of micro-analytical developments. *Fungal Biol Rev* **23**: 122–131.

Strand, J., Kaviani, M., Gao, D., El-Sayed, A.-M., Afanas'ev, V. V., Shluger, A. L. (2018) Intrinsic charge trapping in amorphous oxide films: status and challenges. *J Phys: Condens Matter* **30**: 233001

Sun, F., Polizzotto, M. L., Guan, D., Wu, J., Shen, Q., Ran, W., *et al*. (2017) Exploring the interactions and binding sites between Cd and functional groups in soil using two-dimensional correlation spectroscopy and synchrotron radiation based spectromicroscopies. *J Hazard Mater* **326**: 18–25.

Trusiak, A., Treibergs, L. A., Kling, G. W., and Cory, R. M. (2018) The role of iron and reactive oxygen species in the production of CO_2 in arctic soil waters. *Geochim Cosmochim Acta* **224**: 80–95.

Unger, M., Mattson, E., Patterson, C. S., Alavi, Z., Carson, D., and Hirschmugl, C. J. (2013) Synchrotron-based multiple-beam FTIR chemical imaging of a multi-layered polymer in transmission and reflection: towards cultural heritage applications. *Appl Phys-Mater Sci Proc* **111**: 135–145.

Vanheusden, K., Seager, C. H., Warren, W. L., Tallant, D. R., and Voigt, J. A. (1996) Correlation between photoluminescence and oxygen vacancies in ZnO phosphors. *App Phys Lett* **68**: 403–405.

van Schöll, L., Kuyper, T. W., Smits, M. M., Landeweert, R., Hoffland, E., and Breemen, N. V. (2008) Rock-eating mycorrhizas: their role in plant nutrition and biogeochemical cycles. *Plant Soil* **303**: 35–47.

Voinov, M. A., Pagán, J. O. S., Morrison, E., Smirnova, T. I., and Smirnov, A. I. (2011) Surface-mediated production of hydroxyl radicals as a mechanism of iron oxide nanoparticle biotoxicity. *J Amer Chem Soc* **133**: 35–41.

Wang, X., Dong, H., Zeng, Q., Xia, Q., Zhang, L., and Zhou, Z. (2017) Reduced iron-containing clay minerals as antibacterial agents. *Environ Sci Technol* **51**: 7639–7647.

Wang, Z., Mao, X., Chen, P., Xiao, M., Monny, S. A., Wang, S., *et al*. (2019) Understanding the roles of oxygen vacancies in hematite-based photoelectrochemical processes. *Angew Chem Internat Edit* **58**: 1030–1034.

Wei, H., and Wang, E. (2013) Nanomaterials with enzyme-like characteristics (nanozymes): next-generation artificial enzymes. *Chem Soc Rev* **42**: 6060–6093.

Wei, Z., Hillier, S. and Gadd, G.M. (2012) Biotransformation of manganese oxides by fungi: solubilization and production of manganese oxalate biominerals. *Environ Microbiol* **14**: 1744–1753.

Wen, Y., Xiao, J., Liu, F., Goodman, B. A., Li, W., Jia, Z., *et al*. (2018) Contrasting effects of inorganic and organic fertilisation regimes on shifts in Fe redox bacterial communities in red soils. *Soil Biol Biochem* **117**: 56–67.

Winkler, P., Kaiser, K., Thompson, A., Kalbitz, K., Fiedler, S., and Jahn, R. (2018) Contrasting evolution of iron phase composition in soils exposed to redox fluctuations. *Geochim Cosmochim Acta* **235**: 89–102.

Wu, Y., Jiang, Y., Jiao, J., Liu, M., Hu, F., Griffiths, B. S., and Li, H. (2014) Adsorption of *Trametes versicolor* laccase to soil iron and aluminum minerals: enzyme activity, kinetics and stability studies. *Coll Surf B: Biointerf* **114**: 342–348.

Xiao, J., He, X. H., Hao, J. L., Zhou, Y., Zheng, L. Y., Ran, W., *et al*. (2016) New strategies for submicron characterization the carbon binding of reactive minerals in long-term contrasting fertilized soils: implications for soil carbon storage. *Biogeosciences* **13**: 3607–3618.

Yamashita, T., and Hayes, P. (2008) Analysis of XPS spectra of Fe^{2+} and Fe^{3+} ions in oxide materials. *Appl Surf Sci* **254**: 2441–2449.

Yang, T. Y., Kang, H. Y., Sim, U., Lee, Y. J., Lee, J. H., Koo, B., *et al*. (2013) A new hematite photoanode doping strategy for solar water splitting: oxygen vacancy generation. *Phys Chem Chem Phys* **15**: 2117–2124.

Yang, Z., Kang, J., Li, L., and Guo, L. (2020) A biotemplating route for the synthesis of hierarchical Fe_2O_3 with highly dispersed carbon as electron-transfer channel. *ChemPlusChem* **85**: 258–263.

Yao, S., Jin, B., Liu, Z., Shao, C., Zhao, R., Wang, X., and Tang, R. (2017) Biomineralization: from material tactics to biological strategy. *Adv Mater* **29**: 1605903.

You, Y., Zheng, S., Zang, H., Liu, F., Liu, F., and Liu, J. (2019) Stimulatory effect of magnetite on the syntrophic metabolism of *Geobacte*r co-cultures: Influences of surface coating. *Geochim Cosmochim Acta* **256**: 82–96.

Yu, G. H., Chi, Z. L., Teng, H. H., Dong, H. L., Kappler, A., Gillings, M. R., *et al*. (2019) Fungus-initiated catalytic reactions at hyphal-mineral interfaces drive iron redox cycling and biomineralization. *Geochim Cosmochim Acta* **260**: 192–203.

Yu, G. H., Sun, F. S., Yang, L., He, X. H., and Polizzotto, M. L. (2020) Influence of biodiversity and iron availability on soil peroxide: implications for soil carbon stabilization and storage. *Land Degrad Develop* **31**: 463–472.

Yu, G., Xiao, J., Hu, S., Polizzotto, M. L., Zhao, F., McGrath, S. P., *et al*. (2017) Mineral

availability as a key regulator of soil carbon storage. *Environ Sci Technol* **51**: 4960–4969.

Yuan, S., Liu, X., Liao, W., Zhang, P., Wang, X., and Tong, M. (2018) Mechanisms of electron transfer from structrual Fe(II) in reduced nontronite to oxygen for production of hydroxyl radicals. *Geochim Cosmochim Acta* **223**: 422–436.

Zeng, Q., Huang, L., Ma, J., Zhu, Z., He, C., Shi, Q., *et al.* (2020) Bio-reduction of ferrihydrite-montmorillonite-organic matter complexes: effect of montmorillonite and fate of organic matter. *Geochimi Cosmochim Acta* **276**: 327–344.

Zhang, J., Miao, Y., Rahimi, M. J., Zhu, H., Steindorff, A., Schiessler, S., *et al.* (2019) Guttation capsules containing hydrogen peroxide: an evolutionarily conserved NADPH oxidase gains a role in wars between related fungi. *Environm Microbiol* **21**: 2644–2658.

Zhang, R., Fan, K., and Yan, X. (2020) Nanozymes: created by learning from nature. *Sci China Life Sci*, doi: 10.1007/s11427-019-1570-7.

Zhu, T., Lu, X., Liu, H., Li, J., Zhu, X., Lu, J., and Wang, R. (2014) Quantitative X-ray photoelectron spectroscopy-based depth profiling of bioleached arsenopyrite surface by *Acidithiobacillus ferrooxidans*. *Geochim Cosmochim Acta* **127**: 120–139.

Figure Legends

Fig. 1. Changes with time in (a) pH, (b) dissolved Fe, (c) dissolved Fe(II), (d) total Fe(II), (e) structural Fe(II) and (f) mean particle size in solution during fungus and mineral cultivation. *T.* + Mt, *T. guizhouense* plus magnetite; Mt, magnetite alone; *T.*, *T. guizhouense* alone; pH control, Mt was cultivated with HCl under a pH of ~2.2; 2 G, 10 G and 20 G are the concentrations of glucose (G) in the medium set to 2 g/L, 10 g/L and 20 g/L during *T.* + Mt cultivation and HEPES buffer was also used to control a pH of ~ 7.0. Data are shown as means ± S.D. (n = 3).

Fig. 2. Time curves of the TMB colorimetric reaction catalyzed by magnetite (Mt) during fungus-mineral cultivation. TMB, 3,3',5,5'-tetra-methylbenzidine.

Fig. 3. Catalytic activity of Mt nanoparticles during fungus-mineral cultivation. (a) Peroxidase-like activity. (b) HTPA concentration. (c) HTPA concentration in the extracted Mt particles (1%) from *T.* + Mt treatment, which were cultivated with H_2O_2 (5 µM) in the presence of TPA (2.5 mM) for 2 h. (d) Correlation between peroxidase-like activity and HTPA concentration. *T.* + Mt, *T. guizhouense* plus magnetite; Mt, magnetite alone; *T.*, *T. guizhouense* alone. Data are shown as means ± S.D. (n = 3).

Fig. 4. High-resolution Fe $2p_{3/2}$ (a,c) and O 1s (b,d) XPS spectra of magnetite at the cultivation times of (a,b) 0 h and (c,d) 120 h, respectively. XPS, X-ray photoelectron spectroscopy. Note that the peaks at 530.0 eV and 533.2 eV are assigned to lattice oxygen (O_L) and non-lattice oxygen (O_{NL}), respectively.

Fig. 5. Correlative SEM and NanoSIMS images of fungal-Mt samples after 120 h cultivation. (a) SEM. (b) $^{12}C^{14}N^-$ image. (c) $^{16}O^-$ image. (d) $^{56}Fe^{16}O^-$ image. (e) Composite image of Fe ($^{56}Fe^{16}O^-$, red) and O ($^{16}O^-$, green). (f) Composite image of CN ($^{12}C^{14}N^-$, blue) and Fe ($^{56}Fe^{16}O^-$, red). (g) Composite image of CN ($^{12}C^{14}N^-$, blue), Fe ($^{56}Fe^{16}O^-$, red) and O ($^{16}O^-$, green). (h) Line profile derived from the NanoSIMS images, with a position shown in (a). Note that the colour intensity calibration bar displayed in the chemical maps corresponds to the relative concentrations of individual elements, but cannot be used to compare one element with another.

Fig. 6. Synchrotron radiation based FTIR spectromicroscopy of the thin section (1 µm-thickness) from the fungal-Mt sample after 120 h cultivation. (a) Optical image. (b) Three-dimensional micro-FTIR (µ-FTIR) spectra of the red arrow in (a) with a step of 2 µm. (c) Two-dimensional µ-FTIR spectra of the red arrow in (a) with a step of 2 µm. Note that the distance 0 µm in the stack of µ-FTIR spectra is the start point of the red arrow in (a). The fungus and mineral are differentiated by their unique functional groups.

(d) Individual μ-FTIR spectra. The colour scale in (c) is a relative scale for each peak height and does not allow quantitative comparison between peaks.

Fig. 7. Proposed catalytic mechanisms of fungus produced magnetite nanoparticles acting as a nanozyme. (a) The conventional view is that iron acts as the sole redox-active centre. (b) The alternative mechanism proposed here considers the contribution of both Fe and O to the catalytic activity of Mt nanoparticles, highlighting that surface oxygen anions play a major role in controlling the catalytic activity of the iron nanoparticles.

Supporting Information

Additional Supporting Information may be found in the online version of this article at the publisher's web-site:

Supporting Materials and methods

Fig. S1. Micro-environmental pH measurements of hyphae in the *T. guizhouense* + Mt treatment. Samples were stained with 5 μM SNARF4F (Invitrogen) and observed by confocal laser scanning microscopy using emissions at 580 and 640 nm, after excitation with a 488 nm argon laser.

Fig. S2. Particle size distibution by number in solution during fungus-mineral cultivation.

Fig. S3. Particle size distibution by number in samples after ultrosound treatment (20 kHz and 120W for 10 min) during fungus-mineral cultivation.

Fig. S4. Changes in mean particle size in samples after ultrasound treatment (20 kHz and 120W for 10 min) during fungus and mineral cultivation.

Fig. S5. SR-FTIR mapping of a thin section (1 µm) from fungal-mineral samples after 120 h cultivation. (a) Optical photograph showing the entanglement of Mt during fungal aggregation. (b) SR-FTIR spectromicroscopy demonstrating the presence of iron minerals (Fe-OH, 3450 cm^{-1}; Fe-O, 860 cm^{-1}) in fungal-mineral samples. Typical images are shown from several examinations.

Fig. S6. TEM images (a,d,g,j), high resolution TEM observations (b,e,h,k) and selected area electron diffraction (SAED) patterns (c,f,I,l) of (a-c) original magnetite (Mt) and (d-f) Mt cultivation for 120 h with *T. guizhouense*.

Fig. S7. X-ray powder diffraction patterns. Analyses were performed on original magnetite (Mt) (blue line) and fungus-Mt samples after 120 h cultivation (wine line).

Fig. S8. Fe 2p XPS spectra of magnetite (Mt) (black line) and fungus-Mt samples after 120 h cultivation (red line).

Fig. S9. C 1s XPS spectra of fungus-Mt samples after 0 h and 120 h cultivation.

Fig. S10. EPR spectra of Mt nanoparticles after cultivation with *Trichoderma guizhouense* for different periods of time. Note that the resonance signal of $g = 2.002$, denoted as purple dashed line, corresponds to the singly ionized oxygen vacancy (Vo^+).

Fig. S11. Correlative SEM and NanoSIMS images of fungal-Mt samples after 120 h cultivation. Note that Figure S5 and Figure 5 are two replicate samples. (a) SEM. (b) $^{12}C^{14}N^-$ image. (c) $^{16}O^-$ image. (d) $^{56}Fe^{16}O^-$ image. (e) Composite image of Fe ($^{56}Fe^{16}O^-$, red) and O ($^{16}O^-$, green). (f) Composite image of CN ($^{12}C^{14}N^-$, blue) and Fe ($^{56}Fe^{16}O^-$, red). (g) Composite image of CN ($^{12}C^{14}N^-$, blue), Fe ($^{56}Fe^{16}O^-$, red) and O ($^{16}O^-$, green). (h) Line profile derived from the NanoSIMS images, with the position shown in (a). Note that the colour intensity calibration bar displayed in the chemical maps corresponds to the relative concentrations of individual elements, but cannot be used to compare one element with another.

Fig. S12. Micro-FTIR (µ-FTIR) analysis of a thin section (1 µm-thick) from cultivation of *T. guizhouense* alone (120 h). (a) Optical image. (b) Three-dimensional µ-FTIR spectra of the red arrow in (a) with a step of 2 µm. (c) Two-dimensional µ-FTIR spectra of the red arrow in (a) with a step of 2 µm. Note that the distance 0 µm in the stack of µ-FTIR spectra is the start point of the red arrow in (a). The fungus and mineral are differentiated by their unique functional groups. (d) Individual µ-FTIR spectra. The

colour scale in (c) is a relative scale for each peak height and does not allow quantitative comparisons between peaks.

Table S1. Changes in the Fe(II)/Fe(III) ratio with time during the different cultivation experiments.

Table S2. Gupta and Sen (GS) multiplet peak parameters used to fit high-resolution Fe 2p$_{3/2}$ spectra of pure magnetite (Mt) and *T. guizhouense* + Mt after 120 h cultivation.

Table S3. Deconvolution results of O 1s XPS spectra for pure magnetite (Mt) and *T. guizhouense* + Mt after 120 h cultivation.
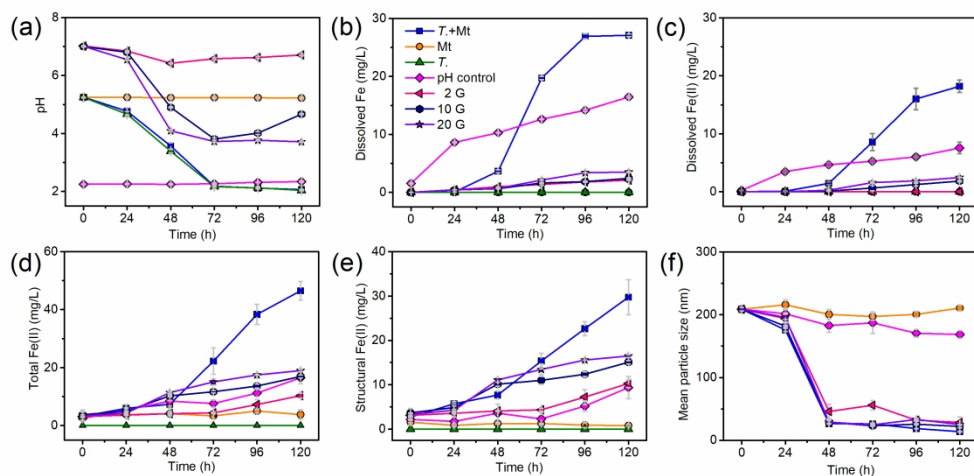
Fig. 1. Changes with time in (a) pH, (b) dissolved Fe, (c) dissolved Fe(II), (d) total Fe(II), (e) structural Fe(II) and (f) mean particle size in solution during fungus and mineral cultivation. T. + Mt, T. guizhouense plus magnetite; Mt, magnetite alone; T., T. guizhouense alone; pH control, Mt was cultivated with HCl under a pH of ~2.2; 2 G, 10 G and 20 G are the concentrations of glucose (G) in the medium set to 2 g/L, 10 g/L and 20 g/L during T. + Mt cultivation and HEPES buffer was also used to control a pH of ~ 7.0. Data are shown as means ± S.D. (n = 3).

278x136mm (300 x 300 DPI)
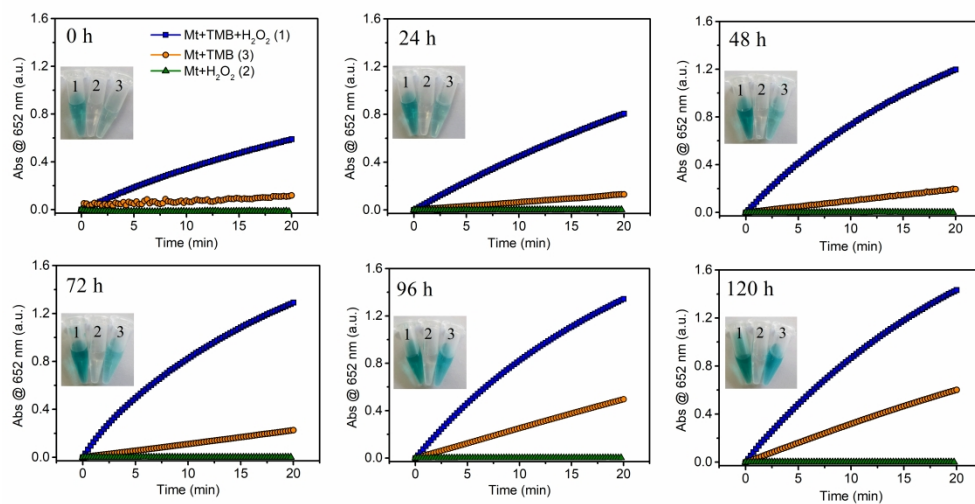
Fig. 2. Time curves of the TMB colorimetric reaction catalyzed by magnetite (Mt) during fungus-mineral cultivation. TMB, 3,3',5,5'-tetra-methylbenzidine.

549x279mm (300 x 300 DPI)
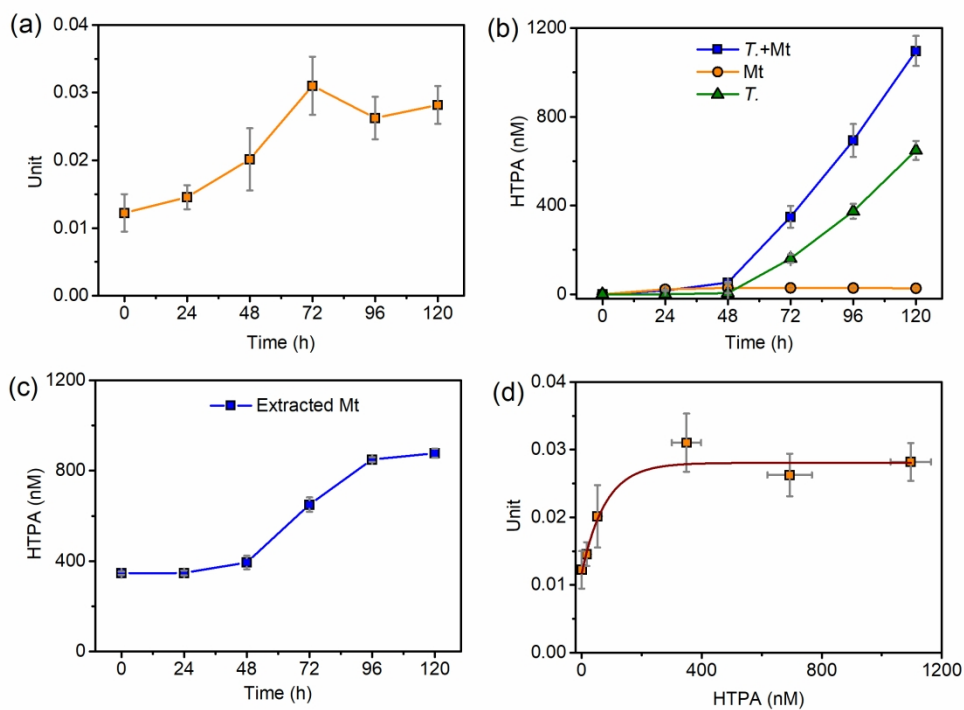
Fig. 3. Catalytic activity of Mt nanoparticles during fungus-mineral cultivation. (a) Peroxidase-like activity. (b) HTPA concentration. (c) HTPA concentration in the extracted Mt particles (1%) from T. + Mt treatment, which were cultivated with H_2O_2 (5 µM) in the presence of TPA (2.5 mM) for 2 h. (d) Correlation between peroxidase-like activity and HTPA concentration. T. + Mt, T. guizhouense plus magnetite; Mt, magnetite alone; T., T. guizhouense alone. Data are shown as means ± S.D. (n = 3).

197x145mm (300 x 300 DPI)
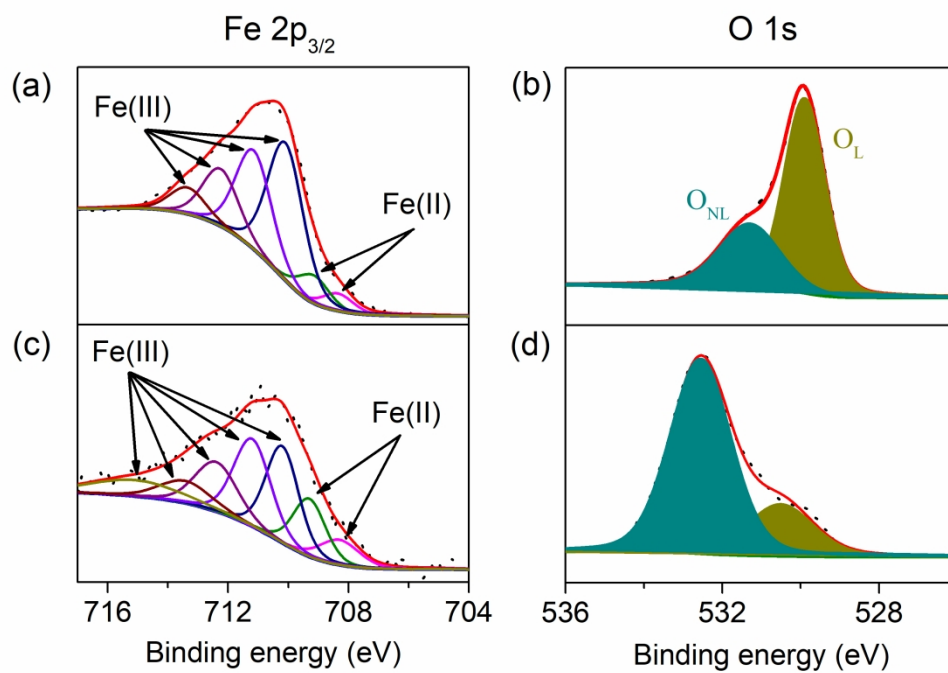
Fig. 4. High-resolution Fe 2p3/2 (a,c) and O 1s (b,d) XPS spectra of magnetite at the cultivation times of (a,b) 0 h and (c,d) 120 h, respectively. XPS, X-ray photoelectron spectroscopy. Note that the peaks at 530.0 eV and 533.2 eV are assigned to lattice oxygen (OL) and non-lattice oxygen (ONL), respectively.
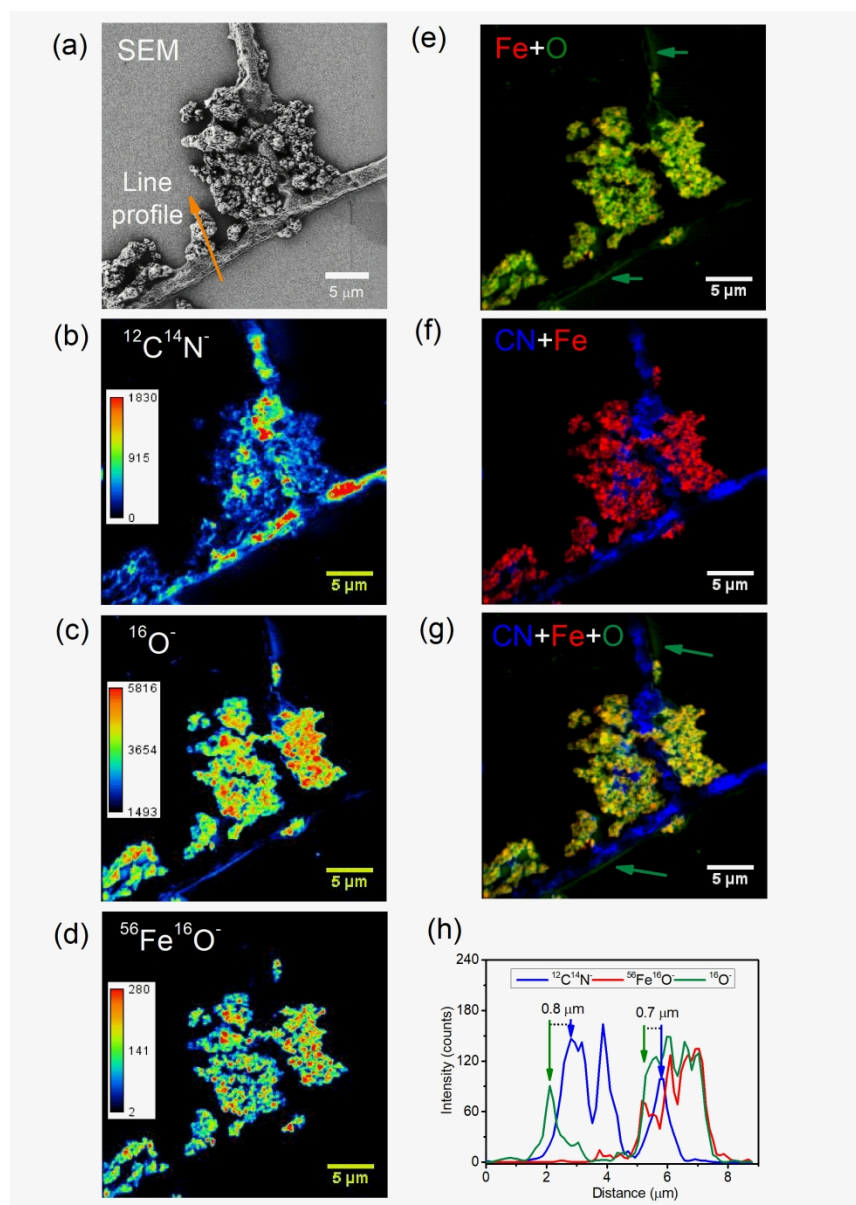
275x194mm (300 x 300 DPI)

Fig. 5. Correlative SEM and NanoSIMS images of fungal-Mt samples after 120 h cultivation. (a) SEM. (b) 12C14N− image. (c) 16O− image. (d) 56Fe16O− image. (e) Composite image of Fe (56Fe16O−, red) and O (16O−, green). (f) Composite image of CN (12C14N−, blue) and Fe (56Fe16O−, red). (g) Composite image of CN (12C14N−, blue), Fe (56Fe16O−, red) and O (16O−, green). (h) Line profile derived from the NanoSIMS images, with a position shown in (a). Note that the color intensity calibration bar displayed in the chemical maps corresponds to the relative concentrations of individual elements, but cannot be used to compare one element with another.
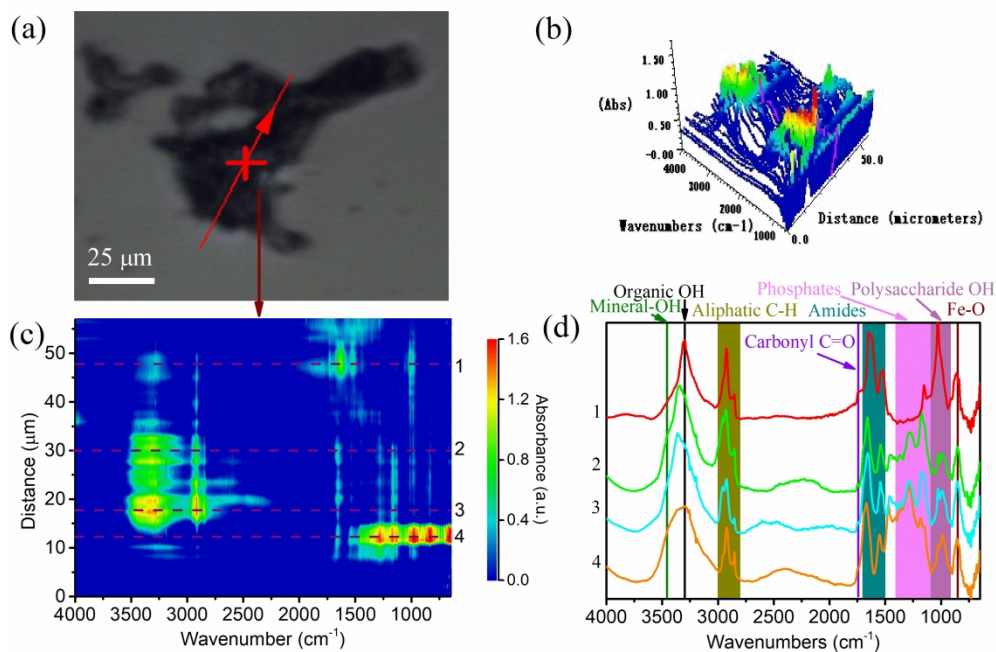
209x293mm (300 x 300 DPI)

Fig. 6. Synchrotron radiation based FTIR spectromicroscopy of the thin section (1 µm-thickness) from the fungal-Mt sample after 120 h cultivation. (a) Optical image. (b) Three-dimensional micro-FTIR (µ-FTIR) spectra of the red arrow in (a) with a step of 2 µm. (c) Two-dimensional µ-FTIR spectra of the red arrow in (a) with a step of 2 µm. Note that the distance 0 µm in the stack of µ-FTIR spectra is the start point of the red arrow in (a). The fungus and mineral are differentiated by their unique functional groups. (d) Individual µ-FTIR spectra. The colour scale in (c) is a relative scale for each peak height and does not allow quantitative comparison between peaks.
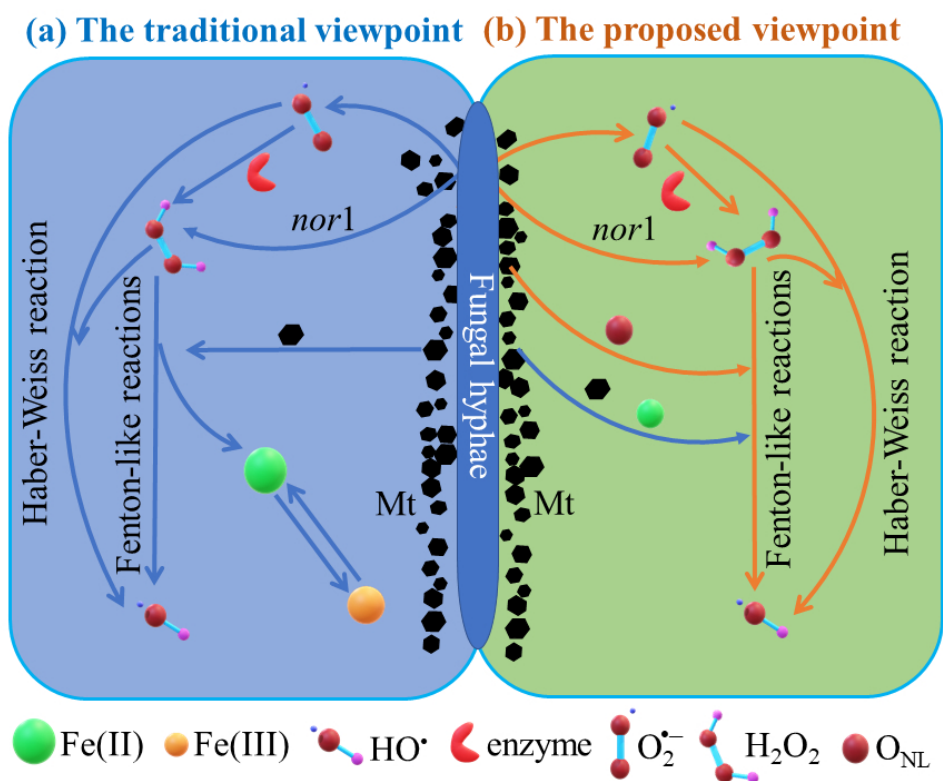
276x185mm (300 x 300 DPI)

Fig. 7. Proposed catalytic mechanisms of fungus produced magnetite nanoparticles acting as a nanozyme. (a) The conventional view is that iron acts as the sole redox-active centre. (b) The alternative mechanism proposed here considers the contribution of both Fe and O to the catalytic activity of Mt nanoparticles, highlighting that surface oxygen anions play a major role in controlling the catalytic activity of the iron nanoparticles.

237x190mm (96 x 96 DPI)